Synthesis, Characterization, and *in Vitro* Testing of Superparamagnetic Iron Oxide Nanoparticles Targeted Using Folic Acid-Conjugated Dendrimers

Kevin J. Landmark,[†,#] Stassi DiMaggio,[▽] Jesse Ward,[⊥] Christopher Kelly,[†,‡,¶,#] Stefan Vogt,[⊗] Seungpyo Hong,[§,#] Alina Kotlyar,[#] Andrzej Myc,[#] Thommey P. Thomas,[#] James E. Penner-Hahn,[‡,⊥] James R. Baker, Jr.,[#] Mark M. Banaszak Holl,[†,‡,§,⊥,#,¶,*] and Bradford G. Orr[†,∥,#,*]

[†]Programs in Applied Physics, [‡]Biophysics, and [§]Macromolecular Science and Engineering, [⊥]Departments of Chemistry and [∥]Physics, [#]the Michigan Nanotechnology Institute for Medicine and Biological Sciences, and [¶]Graham Environmental Sustainability Institute, The University of Michigan, Ann Arbor, Michigan 48109, [▽]Department of Chemistry, Xavier University, New Orleans, Louisiana 70125, and [⊗]X-ray Science Division, Advanced Photon Source, Argonne National Laboratory, Argonne, Illinois 60439

ABSTRACT Organic-coated superparamagnetic iron oxide nanoparticles (OC-SPIONs) were synthesized and characterized by transmission electron microscopy and X-ray photoelectron spectroscopy. OC-SPIONs were transferred from organic media into water using poly(amidoamine) dendrimers modified with 6-TAMRA fluorescent dye and folic acid molecules. The saturation magnetization of the resulting dendrimer-coated SPIONs (DC-SPIONs) was determined, using a superconducting quantum interference device, to be 60 emu/g Fe versus 90 emu/g Fe for bulk magnetite. Selective targeting of the DC-SPIONs to KB cancer cells in vitro was demonstrated and quantified using two distinct and complementary imaging modalities: UV–visible and X-ray fluorescence; confocal microscopy confirmed internalization. The results were consistent between the uptake distribution quantified by flow cytometry using 6-TAMRA UV–visible fluorescence intensity and the cellular iron content determined using X-ray fluorescence microscopy.

KEYWORDS: dendrimers · magnetic nanoparticles · superparamagnetism · phase transfer · targeted MRI contrast agents · X-ray fluorescence microscopy · cancer

Magnetic resonance imaging (MRI) is widely recognized as an important diagnostic technique. Its noninvasive nature and high spatial resolution make it a particularly attractive clinical tool. Contrast in MRI images arises from variations in the relaxation times among water protons caused by differences in the local environment in tissue. Although endogenous variations can afford sufficient contrast to distinguish regions of interest, exogenous contrast agents substantially enhance diagnostic utility.[1–5]

Contrast agents based on chelated paramagnetic ions, such as gadolinium (Gd), and superparamagnetic iron oxide nanoparticles (SPIONs) are currently used in clinical practice.[6–8] For the development of targeted contrast agents, we selected SPIONs based on several key factors. SPIONs exhibit negligible remanence: their magnetization essentially vanishes in the absence of an applied magnetic field. Aggregation concerns due to magnetic interactions are thus minimized; this is especially beneficial for *in vivo* applications.[2,9] The particles' superparamagnetic character also means they exhibit a high saturation magnetization and are effective at concentrations up to 3 orders of magnitude lower than their paramagnetic counterparts: μM Fe versus mM Gd.[1,10] SPION distributions establish magnetic field gradients that alter proton relaxation properties, thus providing a source of contrast for magnetic resonance images. Contrast agents based on Gd rely on exchangeable water molecules to mediate their effects. This difference in the mechanism of action means SPIONs' efficacy as contrast agents is not influenced by their surroundings, whereas the impact of Gd-based agents *in vivo* critically depends on water flux.[11] Lastly, iron oxides do not share the same degree of toxicity concerns as Gd-based contrast agents.[1,12]

Targeting the SPION contrast agents to specifically accumulate in regions of interest greatly enhances their clinical utility.[1,12,13] Various approaches have been employed to achieve this aim. The leaky vasculature and compromised clearance mechanisms within tumors create an enhanced permeation and retention (EPR) effect that allows passive targeting of nanoparticles.[14,15] This approach is limited in scope as it is only useful for solid, nonmetastatic tumors and is heavily dependent upon the degree of capillary

*Address correspondence to mbanasza@umich.edu, orr@umich.edu.

Received for review August 28, 2007 and accepted March 06, 2008.

Published online April 22, 2008.
10.1021/nn800034w CCC: $40.75

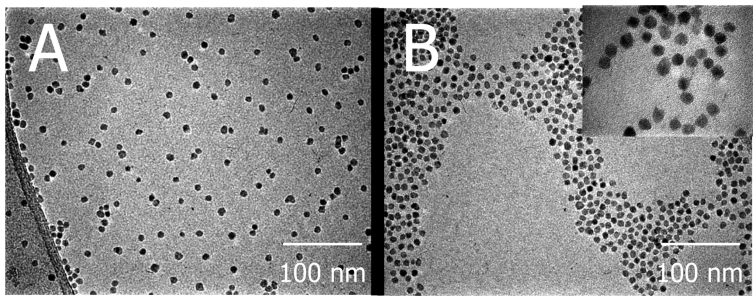

Figure 1. Transmission electron micrographs of magnetite nanocrystals. The OC-SPIONs are shown in (A); panel B displays the DC-SPIONs. The inset of panel B is a higher-resolution image of the same DC-SPIONs clearly showing that size and shape uniformity are maintained. Although drying induces particle grouping, the DC-SPIONs remain isolated and do not form multiparticle aggregates.

endothelial disorder, blood flow, and lymphatic drainage rate.[4,16–18] Additionally, success relies upon extended circulation times in the bloodstream. To accomplish this the nanoparticles are typically required to be larger than can be effectively eliminated by the kidney.[19,20]

In addition to exhibiting the EPR effect, tumor cells also present higher concentrations of receptors on their surfaces related to their enhanced mitosis rates. These receptors can be targeted to effect binding and/or uptake by the tumor cells. Receptors involved in endocytic activity provide an avenue for the particles to be accumulated within the cells instead of being restricted to the surface. Many approaches to active targeting of SPIONs have been documented, including peptides, hormones, antibodies, proteins, therapeutics, and nutrients, such as folic acid (FA).[4,6,12,13,21–32] Antibodies are inherently immunogenic and are also bulky; both properties are believed to inhibit internalization of attached structures.[31] Although none of the other approaches suffer from these particular drawbacks, nutrient pathways are attractive since they are directly linked to proliferation and thus in principle will cause increased uptake of the imaging agent and therefore give greater signal for the most aggressive tumor cells. The folic acid receptor (FAR) is overexpressed in a wide variety of human cancers, as FA is a key precursor in DNA base synthesis and is thus required for tumor cell proliferation.[33,34]

Our group has demonstrated success using poly(amidoamine) (PAMAM) dendrimers conjugated with FA to target tumors both *in vitro* and *in vivo*.[35–43] PAMAM dendrimers are biocompatible, cascade-branched macromolecules with highly flexible surface chemistry that facilitates functionalization. The PAMAM dendrimers used in this work are unique in that the surfaces were completely neutralized by capping with acetyl groups following the covalent attachment of several molecules of both folic acid and 6-TAMRA dye. Folic acid is the targeting moiety; the dye allows optical tracking of the devices, and the neutral surface enhances targeting by minimizing nonspecific interactions with cells.[35,37,44–47] Targeting efficacy is further augmented by the multivalent effect—multiple FA moieties simultaneously interacting with multiple receptors—exhibited by the dendrimer-FA conjugates.[36]

In this paper we demonstrate that appropriately functionalized generation 5 PAMAM (G5) dendrimers are effective phase transfer agents for SPIONs from organic media to water. The dendrimers act as stabilizers for the magnetite nanoparticles, provide a means to target the particles to cells, and impart an alternative fluorescence imaging modality. Selective binding and uptake into KB tumor cells was demonstrated by two distinct and complementary methods. Flow cytometry analysis, following the 6-TAMRA dye conjugated to the dendrimer, confirmed binding of the dendrimer-functionalized SPIONs (DC-SPIONs). X-ray fluorescence (XRF) microscopy quantitatively verified the specific targeting of iron oxide nanoparticles to the KB cells. Confocal microscopy images, including *z*-stacks, verified that the DC-SPIONs were internalized in a manner similar to the free targeted dendrimers. Previous studies either did not quantify iron uptake[6,21,23–27] or did so on bulk samples.[12,13,28–32] This study is unique in demonstrating and quantifying uptake of DC-SPIONs at the single-cell level using the XRF microscopy technique. Such analysis confirms specific targeting of DC-SPIONs and reveals fascinating features and variations that cannot be discerned by bulk analysis.

RESULTS AND DISCUSSION

Nanoparticle Synthesis and Surface Modification. The TEM micrograph in Figure 1A shows the structural characteristics of the magnetite nanoparticles as synthesized in organic media;[48] the particles are consistent in size and shape with a mean diameter of 7.6 $\pm$ 0.7 nm (relative standard deviation of 8.9% for $n = 72$). Such uniformity is desirable since it facilitates determination of the connection between the individual particles and their collective behavior. This is especially useful when evaluating their suitability for use in biological applications. Our novel phase-transfer method leverages the benefits of nanocrystal synthesis in organic solvents, namely superior control over phase, shape, size, and size distribution, and provided a single step to achieving water solubility and enhanced functionality. This is accomplished using G5 dendrimers functionalized with an average of 102 acetamide groups (Ac), 5 molecules of FA, and 3 molecules of 6-TAMRA dye (6T): G5-Ac(102)-FA(5)-6T(3).

We hypothesize that the dendrimers effect phase transfer by displacing the fatty acid ligands whose carboxylate groups are initially coordinated to the OC-SPIONs' surfaces.[49] Since every folic acid moiety on the surrounding dendrimers has a free carboxylate group and there are multiple folic acids per dendrimer, the free carboxylates of some of the folic acid groups likely

accomplish this suface exchange and coordinate to the surface through multidentate interactions. Such a linkage between nanoparticle and dendrimer would be consistent with the many literature examples of carboxylates coordinating to the surfaces of nanoscale metal oxides.[50–53] Furthermore, our parallel attempts to produce a control particle using acetylated dendrimers functionalized with 6-TAMRA but without folic acid failed to yield stable, water-soluble SPIONs: G5-Ac(107)-6T(3) did not produce successful phase transfer, whereas treatment with G5-Ac(102)-FA(5)-6T(3) did.

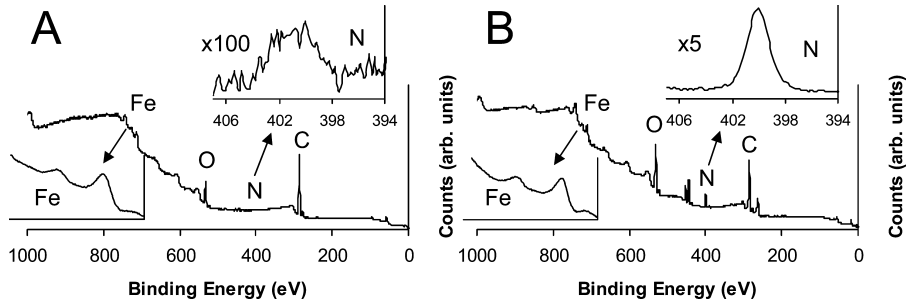

Figure 2. X-ray photoelectron spectroscopy survey scans of (A) OC-SPIONs and (B) DC-SPIONs. The insets demonstrate that although no significant changes occur in the iron region of the spectra, there is a tremendous increase in nitrogen signal from scan A to scan B, corresponding to dendrimers displacing the organic shell and binding to the nanoparticles' surfaces. Analysis of the nitrogen 1s and iron 2p core levels indicates an approximately 20:1 ratio of dendrimers to nanoparticles.

Figure 1B clearly demonstrates that the magnetite nanoparticles' structural quality is maintained upon treatment with G5-Ac(102)-FA(5)-6T(3) and dispersion in water. It is important to note that there is no guarantee of size and shape uniformity being maintained upon phase transfer. Indeed, the concerns of phase transfer operations and place exchange reactions are that significant aggregation and/or changes in particle size and shape can occur.[54–56] The inset gives a clearer indication that the particles do not form fused aggregates even after drying in air. Further evidence that the iron oxide cores remain isolated was demonstrated by lyophilizing and redissolving an aliquot of the aqueous DC-SPION suspension.

The solubility properties of the particles provide strong evidence of surface modification by the hydrophilic dendrimers. Comparing the XPS spectra for the OC-SPIONs and the DC-SPIONs provides further support for this conclusion. Figure 2 depicts survey scans for the capped magnetite cores both before (Figure 2A) and after (Figure 2B) the phase-transfer reaction with G5-Ac(102)-FA(5)-6T(3). The iron regions of both scans are nearly identical, but their nitrogen signatures differ significantly. Although the nitrogen spectrum in Figure 2A shows little more than noise, the same region in Figure 2B displays a strong signal attributed to the over five-hundred nitrogens in the amides and amines that compose the dendrimer backbone. No distinct peaks are seen for the heterocyclic nitrogens in the conjugated folic acid molecules either for the coated particles or even for neat G5-Ac(102)-FA(5)-6T(3). This is not surprising considering the approximately 100:3 theoretical ratio of aliphatic to heterocyclic nitrogen atoms and the expected overlap of the nitrogen 1s core levels.[57]

Magnetic Properties. For their ultimate use as targeted contrast agents for MRI, it is critical that the iron oxide nanoparticles retain their favorable magnetic properties after coating them with dendrimers. The TEM results from Figure 1B demonstrate that the sizes of the DC-SPIONs are unchanged from the OC-SPIONs and that the particles do not form fused aggregates, strongly suggesting that their magnetic properties would be unchanged. SQUID data (Figure 3) show that the DC-SPIONs rapidly approach a saturation magnetization of 60 emu/g Fe, compared to the bulk value of 90 emu/g Fe.[58] Their size and the negligible hysteresis observed in their magnetic profile suggest that the DC-SPIONs are superparamagnetic. Neglecting anisotropy and assuming perfect monodispersity permit the DC-SPIONs to be modeled as a collection of magnetic moments whose behavior is described by the Langevin function:

$$M(\mathbf{H}) = M_s\left(\coth\left(\frac{\mu\mathbf{H}}{K_BT}\right) - \frac{K_BT}{\mu\mathbf{H}}\right) \quad (1)$$

where M_s is the saturation magnetization, **H** is the applied magnetic field, k_B is Boltzmann's constant, T is the absolute temperature, and μ is the magnetic moment of a particle in the ensemble.[59,60] A fit of eq 1 to the magnetization data yields the magnetic moment for a DC-SPION on the order of 10^{-16} erg/G or 10^4 μ_B, where μ_B, the Bohr magneton, is 9.3×10^{-21} erg/G. This dem-

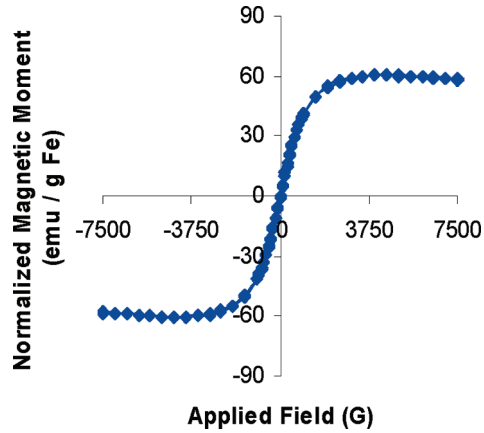

Figure 3. Magnetization curve for DC-SPIONs. The data—taken at 37 °C using a Quantum Design SQUID magnetometer—show that the particles are superparamagnetic with a rapid approach to saturation.

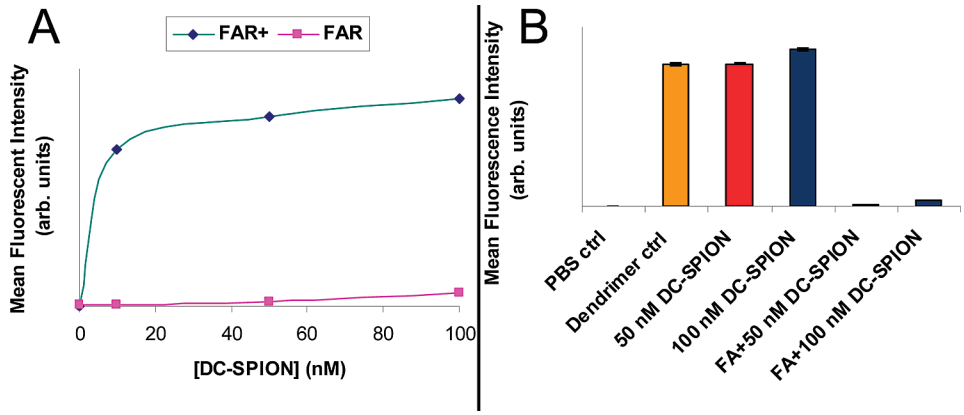

Figure 4. Flow cytometry data for KB cells incubated with DC-SPIONs and the corresponding controls. Error bars indicate the standard error of the mean. Panel A shows binding saturation for KB-FAR+ cells with DC-SPIONs and a slight increase in nonspecific binding for KB-FAR cells over the concentration range. Data in panel B implicate the folate receptor as the binding mediator since cells incubated with free folic acid before DC-SPION addition exhibit significantly reduced fluorescence. Free folic acid added in large excess occupies the cells' receptors for the vitamin and thus inhibits subsequent cell interaction with DC-SPIONs.

onstrates that the particles are superparamagnetic versus merely paramagnetic since paramagnetic moments are generally only a few μ_B.[60] These factors mean the particles are capable of providing substantial contrast in MR images even at modest clinical field strengths.

In-Vitro* Experiments. *KB Cells. KB cells are a human epidermoid carcinoma having a variable level of expression of receptors for the vitamin, folic acid (FA). This variation can be induced by simply varying the concentration of FA in the cells' growth media and allowing time for the cells to adjust. Normal KB cells (KB-FAR) have a minimal expression of the folic acid receptor when maintained in FA-rich media. However, the cells will upregulate their folic-acid-receptor expression when starved of the vitamin.[34,35,41,61] They overexpress the receptor (KB-FAR+) to increase their chances of proliferation. With less FA available in their environment due to its lower presence, competition for the vitamin with other cells, or some combination of factors, KB cells are more likely to survive by enhancing folic-acid-receptor expression. It is interesting to note that the process is dynamic and reversible: normal KB cells can be programmed to upregulate and returned to normal repeatedly by appropriately adjusting the presence of FA in their growth media. These properties make the KB line ideal for use as a tumor model to assess folic-acid-mediated targeting; that is why they were used in this study and in other work done by our group.

UM-SCC-38 Cells. UM-SCC-38 is a squamous cell carcinoma line developed at the University of Michigan that does not express folic acid receptors;[42] therefore, it provides a useful negative control—in addition to normal KB cells—to elucidate the intrinsic binding of DC-SPIONs.

Fluorescence Data. The 6-TAMRA dye molecules present in the DC-SPIONs were used to track particle association with the KB cells over various experimental conditions. Samples were sorted using flow cytometry, and data among groups were compared to investigate receptor-mediated targeting of the devices. The results shown in Figure 4A demonstrate successful targeted binding and/or uptake of the devices as the fluorescence intensity is much higher for KB-FAR+ than for KB-FAR. The saturation seen for KB-FAR+ also suggests site-specific binding versus nonspecific interactions. Similar saturation data were previously observed for the FA-targeted dendrimers alone.[36,40,41] The internal dendrimer control for the current experiments, consisting of G5-Ac(102)-FA(5)-6T(3), showed identical behavior to the DC-SPIONs (Figure 4B). Data from the blocking studies (Figure 4B) confirm site-specific binding and clearly implicate the folate receptor as the means of cell-particle interaction. A vast excess of free folic acid in the growth media prior to treatment with DC-SPIONs occupies the KB cells' FA receptors, thus inhibiting interaction with the FA ligands. The role of FA-receptor targeting was further explored by conducting a comparative study using the KB cell line and a cell line that does not express FA receptors, UM-SCC-38.[42] The KB-FAR+ cells showed a 5.7-fold increase in mean fluorescence, whereas the UM-SCC-38 cells showed no increase in mean fluorescence.

Iron Content Analysis. XRF microscopy was used to determine cellular iron content and to confirm that targeting of the DC-SPIONs caused enhanced binding and/or uptake of iron into the cells as opposed to only binding and/or uptake of the dendrimers themselves. The mean data for 17 cells in each group are summarized in Figure 5. KB-FAR+ cells clearly had the highest iron loading while KB-FAR+ blocked and the blank control were the lowest and exhibited identical content to within experimental error. One picogram of iron translates to approximately 10^6 particles and—assuming a cell volume of 3.5 pL—a corresponding average cellular concentration of ~475 nM particles or ~5 mM Fe. For the 50 nM KB-FAR+ DC-SPION condition this means that between 5 and 10% of the available iron as nanoparticles was bound to or taken up by the cells.

In this study, we report on two methods for measuring the uptake of the DC-SPIONs into the cells and quantification at the individual cell level in both cases. Receptor-mediated targeting of DC-SPIONs is strongly supported by both iron XRF microscopy and

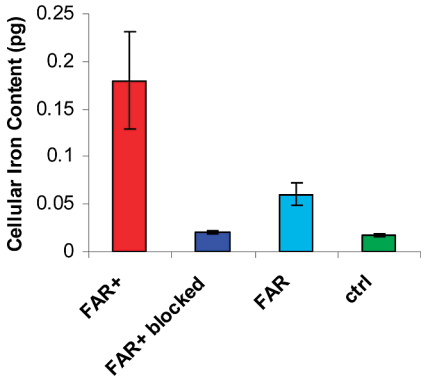

Figure 5. Average cellular iron content as determined by XRF microscopy for different samples. Error bars indicate the standard error of the mean. The largest amount of DC-SPIONs was clearly delivered to KB-FAR+ cells. As expected from the flow cytometry data, KB-FAR cells exhibited significantly lower iron content than KB-FAR+ cells although the level was higher than that of KB-FAR+ blocked cells and the blank control. Statistical analysis using Mann–Whitney U tests showed the iron contents of the KB-FAR+ and KB-FAR+ blocked populations and the KB-FAR+ and control populations to be significantly different with 99% confidence. Similarly, the iron contents of the KB-FAR+ and KB-FAR populations are significantly different with 80% confidence. Taken together, these data demonstrate targeting mediated by the folic acid receptor of the DC-SPIONs to tumor cells.

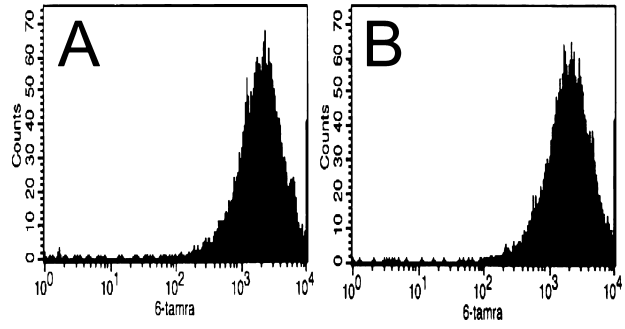

Figure 7. Flow cytometry data distributions for G5-Ac(102)-FA(5)-6T(3) alone (A) and for the same dendrimers coupled to magnetite nanoparticles, DC-SPION (B). Note that the abscissa is a log scale for 6-TAMRA fluorescent intensity, and the ordinate is a linear scale for counts. The distributions are quantitatively identical and reveal a large variation in binding through their ~75% relative standard deviations.

6-TAMRA fluorescence. Details for the entire collection of cells analyzed using XRF microscopy are shown in Figure 6. A striking aspect of this figure is the large degree of variation in iron content per cell. However, this degree of variation is consistent with the distribution of uptake measured for the large populations of cells by flow cytometry as shown in Figure 7. Although direct comparisons between XRF microscopy and flow cytometry data are complicated by several factors, it is still useful to numerically express and analyze the widths of the data distributions observed from these two techniques in this study, to at least illustrate qualitative similarities in their variations. The range of the average values for uptake as measured by fluorescence intensity is typically given as the standard error of the mean (SEM). For the data reported in Figure 7 this yields 2400 ± 20 (0.83% relative SEM, n = 9385) and 2400 ± 20 (0.83% relative SEM, n = 9324) for the targeted dendrimer alone and for the DC-SPIONs, respectively. However, considering the standard deviations (SD) of these data one obtains 2400 ± 1800 (75% relative SD) and 2400 ± 1800 (75% relative SD). The relative SEM and relative SD for the DC-SPIONs from the flow data can be compared to that obtained by XRF microscopy for the 17 KB-FAR+ cells, which are 28% (180 ± 50 fg Fe/cell) and 100% (200 ± 200 fg Fe/cell), respectively. The elevated values for the SEM and SD for the XRF microscopy experiments versus the flow cytometry experiments are attributable to the much smaller number of cells measured by this method as compared to flow cytometry. Nonparametric methods are required for statistical analysis since our sample sizes are small and fail both the F-test for equal variances and the Shapiro−Wilks test for normality. Mann–Whitney U tests reveal that the KB-FAR+ population's iron content is significantly different from those of the KB-FAR+ blocked, KB-FAR, and control populations with 99%, 80%, and 99% confidence, respectively.

Mindful of the data distribution, it is interesting to compare representative XRF microscopy images (iron maps) for cells from each population as de-

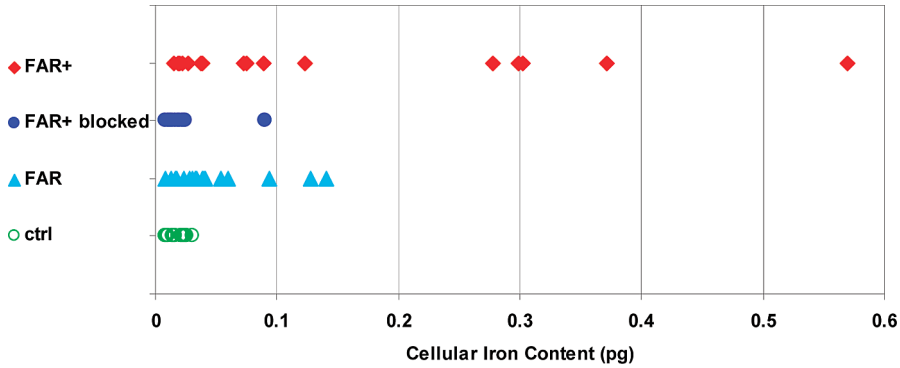

Figure 6. Iron content in femtograms for the 17 cells from each experimental group of 50 nM DC-SPION incubation analyzed by XRF microscopy.

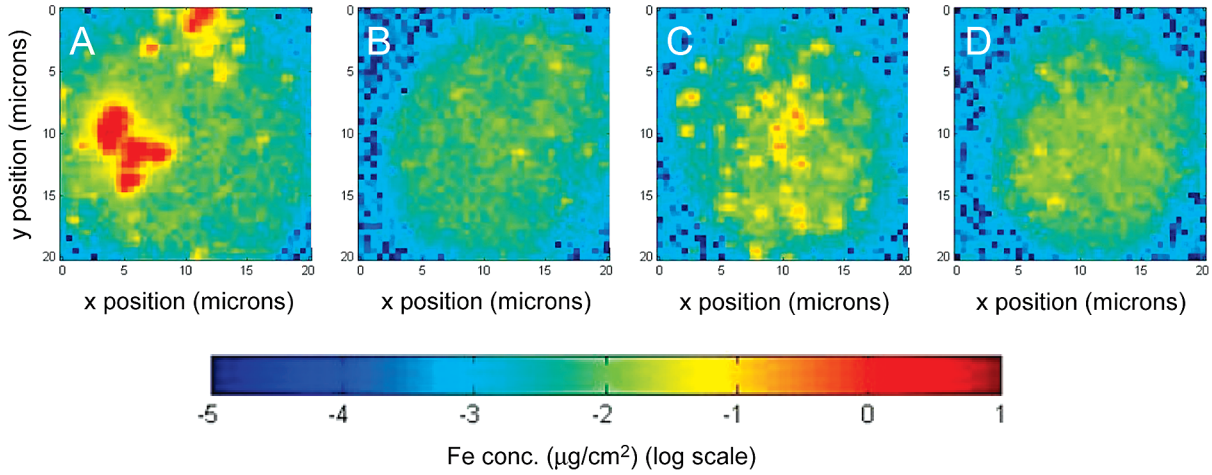

Figure 8. Representative false-color XRF microscopy images showing iron content for a KB cell from each of four populations: (A) KB-FAR+ with 50nM DC-SPIONs, (B) KB-FAR+ with 50nM DC-SPIONs + free FA, (C) KB-FAR with 50nM DC-SPIONs, and (D) untreated control. All incubations were for 1 h. The qualitative feature of localized points of high iron concentration in (A) is obvious; these pockets overwhelm the signal from the cell's endogenous iron background.

picted in Figure 8. Hot spots—localized masses of iron—that are substantially greater than the cell's inherent iron content are evident in the upregulated cells (Figure 8A). All upregulated cells with high nanoparticle content display these hot spots, whereas similar KB-FAR+ blocked (Figure 8B) and KB-FAR (Figure 8C) cells show less localized distributions. The punctate distribution of iron observed in the high-iron KB-FAR+ cells is similar to the clustering of fluorescence seen in the central-slice confocal microscopy images (Figure 9) and suggests DC-SPIONs are contained within intracellular vesicles.[62] Additional evidence for internalization is provided *via* analysis revealing a high autocorrelation between zinc and iron. This is significant since zinc is a transition metal typically associated with the

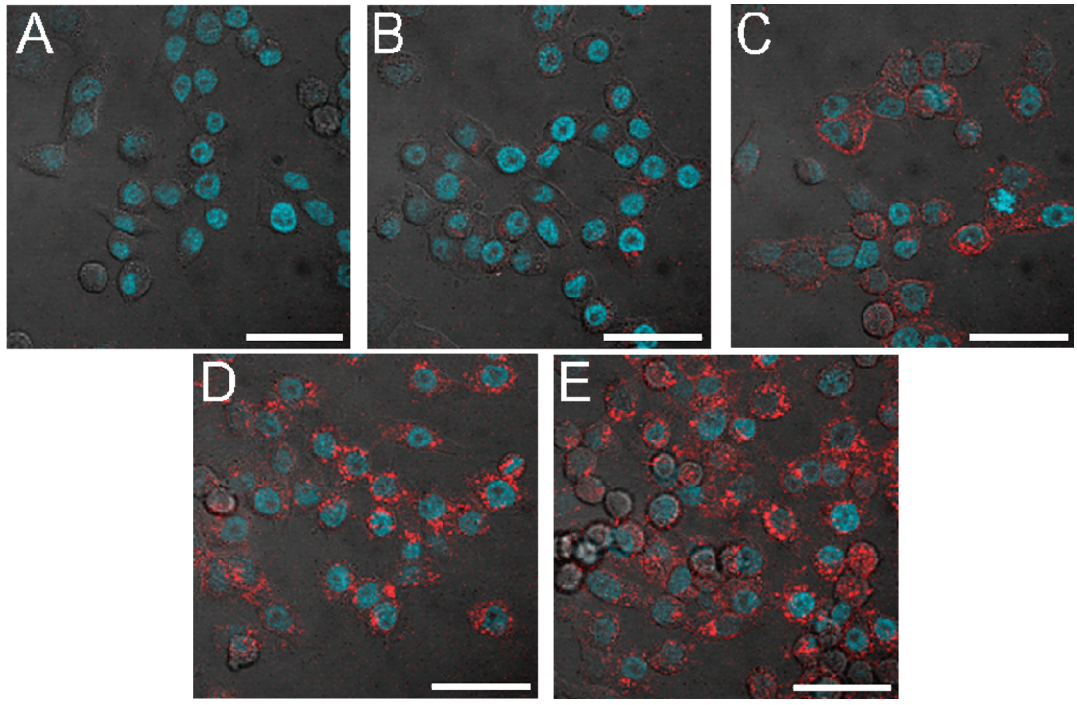

Figure 9. Confocal microscopy images of five experimental conditions demonstrating internalization of DC-SPIONs; scale bars are 40 μm. The slices shown are all from the center of the cells (4 μm from bottom of ~8 μm tall cells) All images are for KB cells after 1 h incubation at 37 °C. Nuclei are visible in blue because of DAPI staining; red fluorescence comes from the 6-TAMRA dye conjugated to neat dendrimers and dendrimers on the surface of DC-SPIONs. The PBS control for KB-FAR+ (A) shows only background fluorescence, and the KB-FAR+ blocked sample (B) exhibits a signal just slightly above this background. Whereas the signal for neat G5-Ac(102)-FA(5)-6T(3) with KB-FAR+ (C) is largely concentrated on the cells' exteriors, the fluorescence for 50 (D) and 100 nM (E) DC-SPIONs is clearly intracellular and appears in clusters, correlating well with the XRF microscopy data for iron.

clathrin-coated pits that are part of the receptor-mediated endocytosis pathway.[63] Furthermore, analysis of *z*-stack confocal microscopy images for 50 nM DC-SPIONs (Figure 10, column A) and 100 nM G5-Ac(102)-FA(5)-6T(3) (Figure 10, column B) shows that the majority of the fluorescence from the nanoparticles occurs in the middle of the cells versus their tops or bottoms. Thus both G5-Ac(102)-FA(5)-6T(3) alone and the composite DC-SPIONs are internalized by the cells.

The data presented in this paper employing DC-SPIONs provide a unique perspective on uptake distribution because iron is quantified on the cellular level and correlated to the entire population of cells characterized by flow cytometry. Previous publications on the topic of targeted delivery of iron oxide particles report intracellular iron content based on acid digestion of bulk samples and subsequent analysis by inductively coupled plasma optical emission spectroscopy (ICP-OES),[28–32] atomic emission spectroscopy (AES),[13] or colorimetric assay.[12] The reported values vary widely. Kresse and co-workers indicate uptake of around 2.8 pg Fe/cell for SPIONs targeted to human epidermoid carcinoma cells (A 431) using the iron chelating protein, transferrin, following 2 h of incubation.[13] Leuschner and collaborators report approximately 150 pg Fe/cell after 30 min of incubating genetically modified human breast cancer cells (MDA-MB-435S) with SPIONs at a concentration of 0.3 mg Fe/mL; the particles accomplished specific binding *via* luteinizing hormone releasing hormone (LHRH) moieties grafted on their surfaces.[12] Finally, Zhang *et al*. have targeted SPIONs using methotrexate (MTX), yielding about 43, 35, and 70 pg Fe/cell for 9L glioma, human cervical adenocarcinoma (HeLa), and human breast cancer cells (MCF-7), respectively, after 2 h of incubation.[28,29] They have also employed folic acid as a ligand to target SPIONs to HeLa and BT20 cells. Uptake of approximately 1.4 pg Fe/cell was achieved for HeLa cells after 4 h of incubation.[30] The first study for BT20 cells showed up to 85 pg Fe/cell after 4 days, while subsequent work yielded around 700 pg Fe/cell over the same period.[31,32] The above set of previously published measurements all characterize iron uptake as an average quantity for a bulk population of cells. We have shown that in our case iron uptake per cell actually varies widely, as would be expected for a FA-targeted system.[35,40,41,44,64] It will be of interest for future studies to see if variation in uptake for magnetic contrast agents is a common behavior for agents targeted to receptors involved in endocytosis mechanisms.

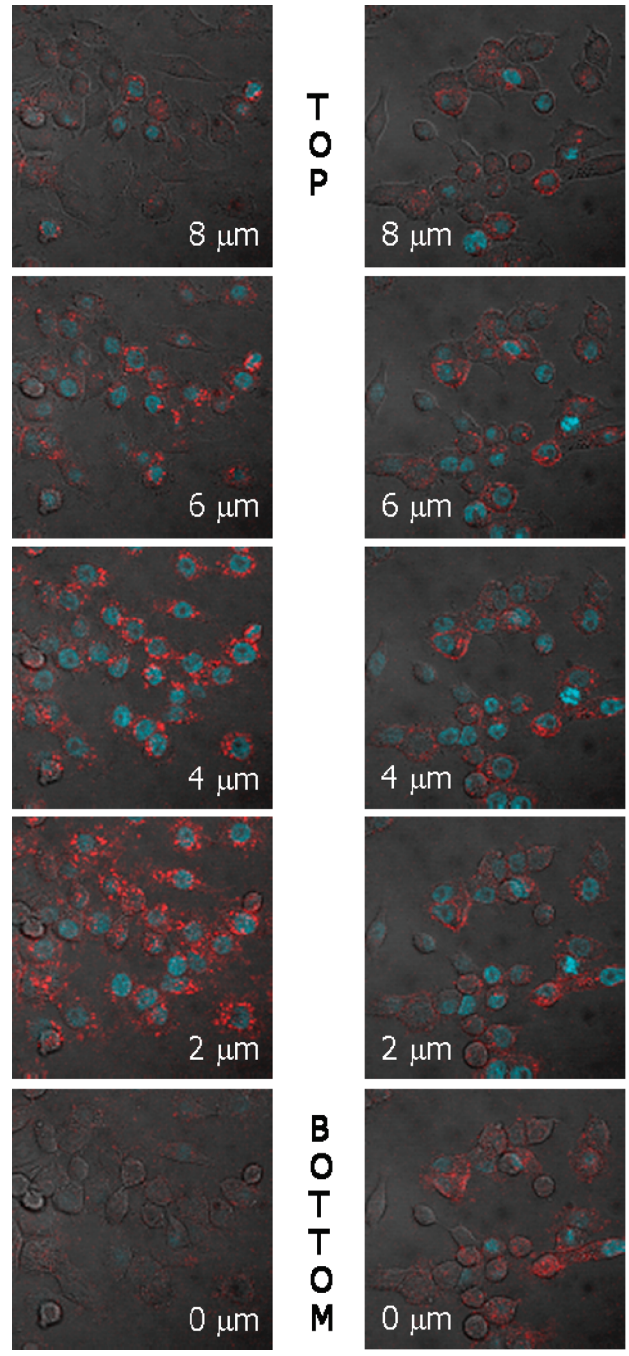

Figure 10. Confocal microscopy *z*-stacks depicting internalization of 50 nM DC-SPIONs (column A); the positive control using neat 100 nM G5-Ac(102)-FA(5)-6T(3) is also shown for comparison (column B). Slices were taken from the sample dish surface (BOTTOM) to the top of the cellular monolayer (TOP); consecutive images in each column are separated by 2 μm. The enhanced fluorescence for the 50 nM DC-SPIONs seen in the middle of the stack shows that the majority of them are within the cells, not bound to the surfaces.

CONCLUSIONS

Functionalized dendrimers were successfully employed to transfer high-quality magnetite nanoparticles from organic to aqueous media. Once biocompatible the nanoparticles retained physical and magnetic properties to establish them as useful contrast agents under clinical conditions. The dendrimer-coated magnetite nanoparticles displayed exceptional stability versus aggregation when stored in water. After drying, they could be readily resuspended in water and could thus be

stored in lyophilized form and dispersed as needed. In addition to affording protection against irreversible aggregation, the dendrimers imparted fluorescent tracking and cellular targeting. Targeting capabilities of the nanoparticle conjugates were verified through the correlation between cellular binding *via* UV–visible (UV–vis) fluorescence for the dendrimers using 6-TAMRA and the iron oxide particles using XRF microscopy.

EXPERIMENTAL SECTION

Reagents and Materials. Reagents were used as obtained from commercial sources. Hexanes (HPLC grade), dimethyl sulfoxide (DMSO, ≥99.8%), methanol (MeOH, HPLC grade), and acetone (≥99.5%) were purchased from Fisher Scientific (Chicago, IL); ProLong Gold with DAPI and 6-carboxytetramethylrhodamine succinimidyl ester (6-TAMRA, 6T) were from Molecular Probes, Inc. (Eugene, OR). Ferric chloride hexahydrate (≥98%) and folic acid (FA, 98%) were acquired from Sigma (St. Louis, MO). Chloroform (≥99.8%), cupferron (97%), acetic anhydride (99.5%), *N*-(3-dimethylaminopropyl)-*N*′-ethylcarbodiimide hydrochloride (EDC, 98%), triethylamine (Et_3N, ≥99.5%), and sodium bicarbonate (>99.5%) were from Sigma-Aldrich (Milwaukee, WI). Epithelial cancer cells of the KB line were obtained from American type Culture Collection (ATCC; Rockville, MD); Dr. J. Mulé at the University of Michigan kindly proffered the head and neck squamous cell carcinoma line, UM-SCC-38.[42] Cell culture media, antibiotics, and supplies were purchased from Gibco BRL (Gaithersburg, MD). Amine-terminated generation 5 PAMAM dendrimers (G5-NH_2) were purchased from Dendritech (Midland, MI) and purified *via* dialysis and ultrafiltration.[39,46] The polymer was checked for the presence of trailing generations by HPLC,[37,65] and characterized by GPC[37,66] and MALDI-TOF[67,68] to establish the molecular weight. The number of primary amine terminal functional groups was determined to be 110 by potentiometric titration.[43,67] Throughout the experiments, ultrapure water with a resistivity of at least 18 MΩ · cm was used as produced by a Milli-Q purification system (Millipore; Bedford, MA).

Dendrimer Conjugation. The PAMAM dendrimers used in this study were modified according to previously published protocols. Acetylation was conducted on G5-NH_2 to neutralize an average of 73% (82 out of 110) of the dendrimers' amine termini to produce G5-Ac(82).[37,66] This step is essential for minimizing nonspecific interactions with cells.[35,37,44–47] Next, EDC coupling was employed to conjugate the targeting moiety, folic acid, at an average of five molecules per dendrimer to yield G5-NH_2(23)-Ac(82)-FA(5).[42,69] 6-TAMRA dye labels were added at 3 equiv per dendrimer primary amine, producing G5-NH_2(20)-Ac(82)-FA(5)-6T(3).[38] Finally, the dendrimers were allowed to react with excess acetic anhydride to convert any remaining surface amines to acetamide groups, resulting in G5-Ac(102)-FA(5)-6T(3).[37,66] Surface functionalization was quantified and purity evaluated following each step using several complementary techniques: peak integrations from proton nuclear magnetic resonance spectroscopy (^{1}H NMR), molecular weight changes from MALDI-TOF mass spectrometry, and using absorbance calibration curves with UV–vis spectroscopy.[36–38,46,65,66]

Magnetite Nanoparticle Synthesis. Magnetite nanoparticles were prepared *via* slight modification of a published procedure involving thermal decomposition of iron cupferron ($FeCup_3$).[48] The $FeCup_3$ precursor was dissolved in octylamine to make a 0.3 M solution. 4.8 mL of this solution was injected into 10.5 mL of a rapidly stirring 0.75 M solution of oleic acid in trioctylamine at 250 °C. After reducing the temperature to 200 °C and aging for 30 min, the clear, black reaction liquid was allowed to cool to room temperature under argon flow. Once cool, stirring was stopped, and a magnet was applied to the flask for 15 min to collect and hold any magnetic precipitate. The supernatant was then magnetically decanted into a new flask and stored under a nitrogen blanket. Aliquots were taken as needed from this stock solution, precipitated using a 3-fold volume excess of acetone and repeatedly washed with acetone *via* magnetic decantation until the supernatant was clear and colorless. The cleaned organic-coated SPIONs (OC-SPIONs) were dried in a nitrogen stream and then dissolved in chloroform for surface modification.

Nanoparticle Surface Modification. A 3.4 mg portion of G5-Ac(102)-FA(5)-6T(3) was dissolved in 1 mL of DMSO. The solution was thoroughly degassed via five cycles of standard freeze–pump–thaw protocol and then placed under flowing Ar. A syringe purged with nitrogen was used to gather a dispersion of 5 mg of OC-SPIONs in 1 mL of chloroform. The dendrimer solution was heated to 75 °C, and the nanoparticles in chloroform were added dropwise at a rate of 1.5 mL/min. After the syringe was emptied, the reaction temperature was reduced to 60 °C, and stirring was continued for 12 h under steady Ar flow. Heat was then removed, and the clear, dark brown/pink liquid product cooled and was transferred to a vial. The dendrimer-coated SPIONs (DC-SPIONs) were isolated from free dendrimer using precipitation and magnetic separation; this purification was performed on individual 150 μL aliquots of the reaction solution to the total volume of ~1.5 mL. A 3-fold volume excess of acetone was added to the aliquot. The mixture was gently agitated, and the resulting precipitate was gathered and held with a magnet while decanting the supernatant. DMSO (150 μL) was added to redissolve the particles. This was followed by precipitation with a 4-fold volume excess of acetone, agitation, and magnetic decantation. The particles were then dried under a nitrogen stream and dissolved in 100 μL of water. The resulting 1 mL of stock solution was determined by inductively coupled plasma optical emission spectroscopy (ICP-OES) to have an iron concentration of 0.66 mg Fe/mL.

Cell Culture. Human epidermoid carcinoma cells (KB) and squamous carcinoma cells (UM-SCC-38) were maintained at 37 °C and 5% CO_2 in RPMI 1640 media supplemented with 10% heat-inactivated fetal bovine serum (FBS) and 1% penicillin/streptomycin. While the UM-SCC-38 cells were maintained in folate-rich media, the KB cell batch was cultured as two distinct populations by growing one-half of the batch in folate-rich media and the other half in folate-deficient media. Although KB cells express the folate receptor in normal media (KB-FAR), the receptor density increases on cells grown in environments with low folic acid concentration (KB-FAR+, upregulated).[34,35,41,61] To study the targeting capabilities of the dendrimer-coated magnetic nanoparticles, KB-FAR, KB-FAR+, and UM-SCC-38 cells were seeded in 24-well plates with 500 μL of serum-free media and allowed to grow into a monolayer over a 48-h period. The neat media were aspirated and replaced by 200 μL media with dendrimer-coated nanoparticle concentrations of 50, 100, and 200 nM in separate wells for 24-h incubation; 200 nM G5-Ac(102)-FA(5)-6T(3) served as the control. Wells for KB-FAR were supplemented with folic acid at a final concentration of 40 μM; blocking studies of KB-FAR+ by free folate were conducted via 15-min preincubation at the same concentration. One-hour incubation was performed the next day using an identical setup on the other halves of the same plates such that the cells from both conditions could be simultaneously harvested. Every condition for the two time points had two replicates: one for flow analysis and the other for iron content measurements. Once incubation was complete, the media were aspirated; the cells were rinsed twice with phosphate-buffered saline (PBS) and were detached by incubating in trypsin-EDTA for 15 min. The content of each well was collected in a separate flow tube with complete media being added to halt trypsin's enzymatic activity. The resulting suspensions were then centrifuged for 5 min at 2000 rpm to form cell pellets. After aspirating the supernatants, 500 μL fresh PBS was added to each tube, and the tubes were agitated to form suspensions before repeating centrifugation. Each tube's supernatant was aspirated, and 500 μL of a 2% buffered paraformaldehyde solution was added to each pellet to fix the cells. The pellets were agi-

tated into suspension and allowed to sit for 15 min before centrifugation. Aspiration, PBS washing, and centrifugation were performed twice before ultimately suspending the fixed cells in 500 μL neat PBS.

Characterization. ***Transmission Electron Microscopy (TEM).*** Specimens for TEM were prepared by releasing a drop of OC-SPIONs in chloroform or a drop of DC-SPION dispersion in water onto 400-mesh copper grids coated by ultrathin carbon support films (Ted Pella; Redding, CA). Once the grids were dry, images were acquired using a Philips CM-12 microscope operating at an accelerating potential difference of 120 kV.

X-ray Photoelectron Spectroscopy (XPS). XPS samples were prepared on substrates cut from a sheet of indium foil (0.127 mm thick, 99.99%; Sigma-Aldrich; Milwaukee, WI). A drop of OC-SPIONs in chloroform or the aqueous DC-SPION dispersion was placed on the foil, and the solvent was allowed to evaporate. Analysis was conducted using an ESCA PHI-5000C (Physical Electronics; Chanhassen, MN) using Mg Kα X-rays (1253.6 eV) and a pass energy of 23.50 eV. Thorough descriptions of the experimental apparatus have been previously published.[70,71]

Superconducting Quantum Interference Device (SQUID) Magnetometry. A Quantum Design (San Diego, CA) MPMS-5 SQUID magnetometer was used to investigate the dependence of sample magnetic moment on applied magnetic field. The specimen was ~30 μL of a concentrated aqueous DC-SPION dispersion in a quartz tube. Residual air was removed from the liquid *via* six cycles of standard freeze–pump–thaw techniques before flame-sealing the tube while under vacuum.

Flow Cytometry. Flow cytometry was conducted at the University of Michigan Cancer Center (Ann Arbor, MI) on a FACSDiVa high-speed cell sorter (Becton, Dickinson & Co.; Franklin Lakes, NJ) using an argon laser to excite the 6-TAMRA labels. Cell samples were prepared for analysis as already described.

Confocal Microscopy. KB-FAR+ cells were plated in glass-bottomed Petri dishes with folate-deficient media. Each dish's media were aspirated and replaced by 500 μL of the appropriate concentration of DC-SPIONs or G5-Ac(102)-FA(5)-6T(3) in serum-free media. Incubation was conducted for 1 h at 37 °C. All media were aspirated; the cells were washed twice with 1 mL of PBS and then fixed by incubation in 1 mL 2% buffered paraformaldehyde for 10 min at room temperature. Aspiration and PBS washing were again conducted twice. After aspirating the final PBS wash, ProLong Gold—an antifade reagent with DAPI to stain nuclei—was added. Confocal experiments were conducted on a Zeiss LSM 510 confocal microscope using a C-Apochromat 63x objective with a 1.2 NA and water immersion. Each image includes a color layer of red fluorescence from the 6-TAMRA, blue fluorescence from the DAPI, and differential interference contrast (DIC) of all cells in view. 6-TAMRA images were acquired using HeNe laser excitation at 543 nm, with emission detected at wavelengths >560 nm. DAPI images were acquired using Ar laser excitation at 364 nm, with emission detected at wavelengths between 385 and 470 nm.

X-ray Fluorescence (XRF) Microscopy. Cell samples for elemental analysis were prepared on silicon nitride (Si_3N_4) windows (membrane thickness: 500 nm; Silson Ltd.; Blisworth, Northampton, England). A drop of fixed cells suspended in PBS was deposited on the window and allowed to dry in a biological safety cabinet. Several water rinses were then conducted to remove salt crystals remaining from the evaporated buffer since the crystals make it difficult to locate target cells in addition to raising the background level of fluorescent X-rays.[72] After thoroughly drying, the Si_3N_4 windows were collected and placed into a desiccator for storage and transportation to the Advanced Photon Source (APS; Argonne, IL). Once at the APS the windows were mounted on kinematic sample holders. Cells of interest were located on the Si_3N_4 windows using a visible light microscope (Leica DMXRE; Leica Microsystems; Wetzlar, Germany) equipped with a motorized, high-precision *x*/*y*-stage (Ludl Bioprecision; Hawthorne, NY). The cells were selected from random locations on the silicon nitride windows and inspected to verify that they had remained intact during sample preparation. Any lysed cells were eliminated as candidates for XRF analysis. Another cell was then randomly selected and observed for integrity until the desired total was reached. It should be noted that there are no evident morphological differences between cells with high iron content versus cells with low iron content. Specimen positions were recorded and used to locate the same cells for elemental analysis *via* X-ray fluorescence on the 2-ID-E beamline at the APS. Samples were illuminated with a 10 keV X-ray beam focused to a 0.3 μm × 0.5 μm spot using Fresnel zone plates (Xradia; Concord, CA). X-ray fluorescence corresponding to elements with atomic number $Z = 13$ (Al) through $Z = 30$ (Zn) was detected using an Ultra-LEGe energy dispersive Ge-detector (Be window thickness: 24 μm; single-element area: 100 mm^2; Canberra; Meriden, CT) as the sample was raster-scanned through the beam spot. A complete X-ray fluorescence spectrum was acquired at every scan position for subsequent processing. Elemental concentrations were calculated using thin-film samples NBS-1832 and NBS-1833 from the National Institute of Standards and Technology (NIST; Gaithersburg, MD) as calibration standards. MAPS software—developed by Stefan Vogt and Martin de Jonge—was used to evaluate all acquired spectra, produce elemental maps, and calculate iron content per cell.[73]

Acknowledgment. Work on this project was supported in part by the National Institutes of Health under Grant No. 5R01EB002657 to James R. Baker, Jr. and Grant No. 5R01GM038047 to James E. Penner-Hahn. Jesse Ward was funded in part by an NIH training grant: No. 5T32GM008270. The TEM used in this study was acquired under Grant No. EAR-8708276 from the National Science Foundation. XRF microscopy data were acquired at beamline 2-ID-E of the Advanced Photon Source. Use of the Advanced Photon Source was supported by the United States Department of Energy, Office of Science, Office of Basic Energy Sciences, under Contract No. DE-AC02-06CH11357.

REFERENCES AND NOTES

1. Artemov, D. Molecular Magnetic Resonance Imaging with Targeted Contrast Agents. *J. Cell. Biochem.* **2003**, *90*, 518–524.
2. Pankhurst, Q. A.; Connolly, J.; Jones, S. K.; Dobson, J. Applications of Magnetic Nanoparticles in Biomedicine. *J. Phys. D: Appl. Phys.* **2003**, *36*, R167–R181.
3. Bulte, J. W. M.; Kraitchman, D. L. Iron Oxide MR Contrast Agents for Molecular and Cellular Imaging. *NMR Biomed.* **2004**, *17*, 484–499.
4. Sunderland, C. J.; Steiert, M.; Talmadge, J. E.; Derfus, A. M.; Barry, S. E. Targeted Nanoparticles for Detecting and Treating Cancer. *Drug Dev. Res.* **2006**, *67*, 70–93.
5. Ito, A.; Shinkai, M.; Honda, H.; Kobayashi, T. Medical Application of Functionalized Magnetic Nanoparticles. *J. Biosci. Bioeng.* **2005**, *100*, 1–11.
6. Choi, H.; Choi, S. R.; Zhou, R.; Kung, H. F.; Chen, I.-W. Iron Oxide Nanoparticles as Magnetic Resonance Contrast Agent for Tumor Imaging via Folate Receptor-Targeted Delivery. *Acad. Radiol.* **2004**, *11*, 996–1004.
7. Lin, S.-P.; Brown, J. J. MR Contrast Agents: Physical and Pharmacologic Basics. *J. Magn. Reson. Imaging* **2007**, *25*, 884–899.
8. Wang, Y.-X. J.; Hussain, S.; Krestin, G. Superparamagnetic Iron Oxide Contrast Agents: Physicochemical Characteristics and Applications in MR Imaging. *Eur. Radiol.* **2001**, *11*, 2319–2331.
9. Lübbe, A. S.; Bergemann, C.; Brock, J.; McClure, D. G. Physiological Aspects in Magnetic Drug-Targeting. *J. Magn. Magn. Mater.* **1999**, *194*, 149–155.
10. Gillies, R. J. In Vivo Molecular Imaging. *J. Cell. Biochem.* **2002**, *87*, 231–238.
11. Lanza, G. M.; Winter, P. M.; Caruthers, S. D.; Morawski, A. M.; Schmieder, A. H.; Crowder, K. C.; Wickline, S. A. Magnetic Resonance Molecular Imaging with Nanoparticles. *J. Nucl. Cardiol.* **2004**, *11*, 733–743.
12. Leuschner, C.; Kumar, C.; Hansel, W.; Soboyejo, W.; Zhou, J.; Hormes, J. LHRH-Conjugated Magnetic Iron Oxide Nanoparticles for Detection of Breast Cancer Metastases. *Breast Cancer Res. Treat.* **2006**, *99*, 163–176.

13. Kresse, M.; Wagner, S.; Pfefferer, D.; Lawaczeck, R.; Elste, V.; Semmler, W. Targeting of Ultrasmall Superparamagnetic Iron Oxide (USPIO) Particles to Tumor Cells In Vivo by Using Transferrin Receptor Pathways. *Magn. Res. Med.* **1998**, *40*, 236–242.
14. Jain, R. K. Transport of Molecules, Particles, and Cells in Solid Tumors. *Annu. Rev. Biomed. Eng.* **1999**, *1*, 241–263.
15. Jain, R. K. Delivery of Molecular Medicine to Solid Tumors: Lessons from In Vivo Imaging of Gene Expression and Function. *J. Controlled Release* **2001**, *74*, 7–25.
16. Moghimi, S. M.; Hunter, A. C.; Murray, J. C. Long-Circulating and Target-Specific Nanoparticles: Theory to Practice. *Pharmacol. Rev.* **2001**, *53*, 283–318.
17. McNeil, S. E. Nanotechnology for the Biologist. *J. Leukocyte Biol.* **2005**, *78*, 585–594.
18. Sinha, R.; Kim, G. J.; Nie, S.; Shin, D. M. Nanotechnology in Cancer Therapeutics: Bioconjugated Nanoparticles for Drug Delivery. *Mol. Cancer Ther.* **2006**, *5*, 1909–1917.
19. Gaucher, G.; Dufresne, M. H.; Sant, V. P.; Kang, N.; Maysinger, D.; Leroux, J. C. Block Copolymer Micelles: Preparation, Characterization and Application in Drug Delivery. *J. Controlled Release* **2005**, *109*, 169–188.
20. Lee, C. C.; MacKay, J. A.; Fréchet, J. M. J.; Szoka, F. C. Designing Dendrimers for Biological Applications. *Nat. Biotechnol.* **2005**, *23*, 1517–1526.
21. Artemov, D.; Mori, N.; Okollie, B.; Bhujwalla, Z. M. MR Molecular Imaging of the Her-2/*neu* Receptor in Breast Cancer Cells Using Targeted Iron Oxide Nanoparticles. *Magn. Res. Med.* **2003**, *49*, 403–408.
22. Bergey, E. J.; Levy, L.; Wang, X.; Krebs, L. J.; Lal, M.; Kim, K.-S.; Pakatchi, S.; Liebow, C.; Prasad, P. N. DC Magnetic Field Induced Magnetocytolysis of Cancer Cells Targeted by LH-RH Magnetic Nanoparticles In Vitro. *Biomed. Microdevices* **2002**, *4*, 293–299.
23. Boutry, S.; Laurent, S.; Elst, L. V.; Muller, R. N. Specific E-Selectin Targeting with a Superparamagnetic MRI Contrast Agent. *Contrast Media Mol. Imaging* **2006**, *1*, 15–22.
24. Hu, F.; Wei, L.; Zhou, Z.; Ran, Y.; Li, Z.; Gao, M. Preparation of Biocompatible Magnetite Nanocrystals for In Vivo Magnetic Resonance Detection of Cancer. *Adv. Mater.* **2006**, *18*, 2553–2556.
25. Huh, Y.-M.; Jun, Y.; Song, H.-T.; Kim, S.; Choi, J. S.; Lee, J.-H.; Yoon, S.; Kim, K.-S.; Shin, J.-S.; Suh, J.-S.;. *et al*. In Vivo Magnetic Resonance Detection of Cancer by Using Multifunctional Magnetic Nanocrystals. *J. Am. Chem. Soc.* **2005**, *127*, 12387–12391.
26. Montet, X.; Weissleder, R.; Josephson, L. Imaging Pancreatic Cancer with a Peptide-Nanoparticle Conjugate Targeted to Normal Pancreas. *Bioconjugate Chem.* **2006**, *17*, 905–911.
27. Nasongkla, N.; Bey, E.; Ren, J.; Ai, H.; Khemtong, C.; Guthi, J. S.; Chin, S.-F.; Sherry, A. D.; Boothman, D. A.; Gao, J. Multifunctional Polymeric Micelles as Cancer-Targeted, MRI-Ultrasensitive Drug Delivery Systems. *Nano Lett.* **2006**, *6*, 2427–2430.
28. Kohler, N.; Sun, C.; Wang, J.; Zhang, M. Methotrexate-Modified Superparamagnetic Nanoparticles and Their Intracellular Uptake into Human Cancer Cells. *Langmuir* **2005**, *21*, 8858–8864.
29. Kohler, N.; Sun, C.; Fichtenholtz, A.; Gunn, J.; Fang, C.; Zhang, M. Methotrexate-Immobilized Poly(ethylene glycol) Magnetic Nanoparticles for MR Imaging and Drug Delivery. *Small* **2006**, *2*, 785–792.
30. Sun, C.; Sze, R.; Zhang, M. Folic Acid-PEG Conjugated Superparamagnetic Nanoparticles for Targeted Cellular Uptake and Detection by MRI. *J. Biomed. Mater. Res., Part A* **2006**, *78A*, 550–557.
31. Zhang, Y.; Kohler, N.; Zhang, M. Surface Modification of Superparamagnetic Magnetite Nanoparticles and Their Intracellular Uptake. *Biomaterials* **2002**, *23*, 1553–1561.
32. Zhang, Y.; Sun, C.; Kohler, N.; Zhang, M. Self-Assembled Coatings on Individual Monodisperse Magnetite Nanoparticles for Efficient Intracellular Uptake. *Biomed. Microdevices* **2004**, *6*, 33–40.
33. Weitman, S. D.; Lark, R. H.; Coney, L. R.; Fort, D. W.; Frasca, V.; Zurawski, V. R., Jr.; Kamen, B. A. Distribution of the Folate Receptor GP38 in Normal and Malignant Cell Lines and Tissues. *Cancer Res.* **1992**, *52*, 3396–3401.
34. Ross, J. F.; Chaudhuri, P. K.; Ratnam, M. Differential Regulation of Folate Receptor Isoforms in Normal and Malignant Tissues In Vivo and in Established Cell Lines: Physiologic and Clinical Implications. *Cancer* **1994**, *73*, 2432–2443.
35. Baker, J. R., Jr.; Quintana, A.; Piehler, L.; Banaszak Holl, M.; Tomalia, D.; Raczka, E. The Synthesis and Testing of Anti-Cancer Therapeutic Nanodevices. *Biomed. Microdevices* **2001**, *3*, 61–69.
36. Hong, S.; Leroueil, P. R.; Majoros, I. J.; Orr, B. G.; Baker, J. R., Jr.; Banaszak Holl, M. M. The Binding Avidity of a Nanoparticle-Based Multivalent Targeted Drug Delivery Platform. *Chem. Biol.* **2007**, *14*, 107–115.
37. Majoros, I. J.; Thomas, T. P.; Mehta, C. B.; Baker, J. R., Jr. Poly(amidoamine) Dendrimer-Based Multifunctional Engineered Nanodevice for Cancer Therapy. *J. Med. Chem.* **2005**, *48*, 5892–5899.
38. Thomas, T. P.; Myaing, M. T.; Ye, J. Y.; Candido, K.; Kotlyar, A.; Beals, J.; Cao, P.; Keszler, B.; Patri, A. K.; Norris, T. B. Detection and Analysis of Tumor Fluorescence Using a Two-Photon Optical Fiber Probe. *Biophys. J.* **2004**, *86*, 3959–3965.
39. Kukowska-Latallo, J. F.; Candido, K. A.; Cao, Z.; Nigavekar, S. S.; Majoros, I. J.; Thomas, T. P.; Balogh, L. P.; Khan, M. K.; Baker, J. R., Jr. Nanoparticle Targeting of Anticancer Drug Improves Therapeutic Response in Animal Model of Human Epithelial Cancer. *Cancer Res.* **2005**, *65*, 5317–5324.
40. Quintana, A.; Raczka, E.; Piehler, L.; Lee, I.; Myc, A.; Majoros, I.; Patri, A. K.; Thomas, T.; Mulé, J.; Baker, J. R., Jr. Design and Function of a Dendrimer-Based Therapeutic Nanodevice Targeted to Tumor Cells Through the Folate Receptor. *Pharm. Res.* **2002**, *19*, 1310–1316.
41. Thomas, T. P.; Majoros, I. J.; Kotlyar, A.; Kukowska-Latallo, J. F.; Bielinska, A.; Myc, A.; Baker, J. R., Jr. Targeting and Inhibition of Cell Growth by an Engineered Dendritic Nanodevice. *J. Med. Chem.* **2005**, *48*, 3729–3735.
42. Myc, A.; Majoros, I. J.; Thomas, T. P.; Baker, J. R., Jr. Dendrimer-Based Targeted Delivery of an Apoptotic Sensor in Cancer Cells. *Biomacromolecules* **2007**, *8*, 13–18.
43. Majoros, I. J.; Myc, A.; Thomas, T.; Mehta, C. B.; Baker, J. R., Jr. PAMAM Dendrimer-Based Multifunctional Conjugate for Cancer Therapy: Synthesis, Characterization, and Functionality. *Biomacromolecules* **2006**, *7*, 572–579.
44. Patri, A. K.; Myc, A.; Beals, J.; Thomas, T. P.; Bander, N. H.; Baker, J. R., Jr. Synthesis and In Vitro Testing of J591 Antibody-Dendrimer Conjugates for Targeted Prostate Cancer Therapy. *Bioconjugate Chem.* **2004**, *15*, 1174–1181.
45. Shukla, R.; Thomas, T. P.; Peters, J.; Kotlyar, A.; Myc, A.; Baker, J. R., Jr. Tumor Angiogenic Vasculature Targeting with PAMAM Dendrimer-RGD Conjugates. *Chem. Commun.* **2005**, 5739–5741.
46. Hong, S.; Bielinska, A. U.; Mecke, A.; Keszler, B.; Beals, J. L.; Shi, X.; Balogh, L.; Orr, B. G.; Baker, J. R., Jr.; Banaszak Holl, M. M. Interaction of Poly(amidoamine) Dendrimers with Supported Lipid Bilayers and Cells: Hole Formation and the Relation to Transport. *Bioconjugate Chem.* **2004**, *15*, 774–782.
47. Leroueil, P. R.; Hong, S.; Mecke, A.; Baker, J. R., Jr.; Orr, B. G.; Banaszak Holl, M. M.; Nanoparticle Interaction with Biological Membranes: Does Nanotechnology Present a Janus Face?, *Acc. Chem. Res.* **2007**, *40*, 335–342.
48. Rockenberger, J.; Scher, E. C.; Alivisatos, A. P. A New Nonhydrolytic Single-Precursor Approach to Surfactant-Capped Nanocrystals of Transition Metal Oxides. *J. Am. Chem. Soc.* **1999**, *121*, 11595–11596.
49. Bronstein, L. M.; Huang, X.; Retrum, J.; Schmucker, A.; Pink, M.; Stein, B. D.; Dragnea, B. Influence of Iron Oleate Complex Structure on Iron Oxide Nanoparticle Formation. *Chem. Mater.* **2007**, *19*, 3624–3632.

50. Harris, L. A.; Goff, J. D.; Carmichael, A. Y.; Riffle, J. S.; Harburn, J. J.; St, T. G.; Saunders, M. Magnetite Nanoparticle Dispersions Stabilized with Triblock Copolymers. *Chem. Mater.* **2003**, *15*, 1367–1377.
51. Lattuada, M.; Hatton, T. A. Functionalization of Monodisperse Magnetic Nanoparticles. *Langmuir* **2007**, *23*, 2158–2168.
52. Kataby, G.; Ulman, A.; Cojocaru, M.; Gedanken, A. Coating a Bola-Amphiphile on Amorphous Iron Nanoparticles. *J. Mater. Chem.* **1999**, *9*, 1501–1506.
53. Kataby, G.; Ulman, A.; Prozorov, R.; Gedanken, A. Coating of Amorphous Iron Nanoparticles by Long-Chain Alcohols. *Langmuir* **1998**, *14*, 1512–1515.
54. Wang, Y.; Teng, X.; Wang, J. S.; Yang, H. Solvent-Free Atom Transfer Radical Polymerization in the Synthesis of Fe_2O_3@Polystyrene Core-Shell Nanoparticles. *Nano Lett.* **2003**, *3*, 789–793.
55. Yu, W. W.; Chang, E.; Sayes, C. M.; Drezek, R.; Colvin, V. L. Aqueous Dispersion of Monodisperse Magnetic Iron Oxide Nanocrystals through Phase Transfer. *Nanotechnology* **2006**, *17*, 4483–4487.
56. Boal, A. K.; Das, K.; Gray, M.; Rotello, V. M. Monolayer Exchange Chemistry of γ-Fe_2O_3 Nanoparticles. *Chem. Mater.* **2002**, *14*, 2628–2636.
57. Cecchet, F.; Pilling, M.; Hevesi, L.; Schergna, S.; Wong, J. K. Y.; Clarkson, G. J.; Leigh, D. A.; Rudolf, P. Grafting of Benzylic Amide Macrocycles onto Acid-Terminated Self-Assembled Monolayers Studied by XPS, RAIRS, and Contact Angle Measurements. *J. Phys. Chem. B* **2003**, *107*, 10863–10872.
58. Liu, X.; Kaminski, M. D.; Guan, Y.; Chen, H.; Liu, H.; Rosengart, A. J. Preparation and Characterization of Hydrophobic Superparamagnetic Magnetite Gel. *J. Magn. Magn. Mater.* **2006**, *306*, 248–253.
59. Kim, D. K.; Zhang, Y.; Kehr, J.; Klason, T.; Bjelke, B.; Muhammed, M. Characterization and MRI Study of Surfactant-Coated Superparamagnetic Nanoparticles Administered into the Rat Brain. *J. Magn. Magn. Mater.* **2001**, *225*, 256–261.
60. Dennis, C. L.; Borges, R. P.; Buda, L. D.; Ebels, U.; Gregg, J. F.; Hehn, M.; Jouguelet, E.; Ounadjela, K.; Petej, I.; Prejbeanu, I. L. The Defining Length Scales of Mesomagnetism: A Review. *J. Phys.: Condens. Matter* **2002**, *14*, R1175–R1262.
61. Leamon, C. P.; Low, P. S. Delivery of Macromolecules into Living Cells: A Method that Exploits Folate Receptor Endocytosis. *Proc. Natl. Acad. Sci. U.S.A.* **1991**, *88*, 5572–5576.
62. Dubé, D.; Francis, M.; Leroux, J. C.; Winnik, F. M. Preparation and Tumor Cell Uptake of Poly(*N*-isopropylacrylamide) Folate Conjugates. *Bioconjugate Chem.* **2002**, *13*, 685–692.
63. Remacle, A.; Murphy, G.; Roghi, C. Membrane Type I-Matrix Metalloproteinase (MT1-MMP) is Internalised by Two Different Pathways and is Recycled to the Cell Surface. *J. Cell Sci.* **2003**, *116*, 3905–3916.
64. Thomas, T. P.; Patri, A. K.; Myc, A.; Myaing, M. T.; Ye, J. Y.; Norris, T. B.; Baker, J. R., Jr. In Vitro Targeting of Synthesized Antibody-Conjugated Dendrimer Nanoparticles. *Biomacromolecules* **2004**, *5*, 2269–2274.
65. Islam, M. T.; Shi, X.; Balogh, L.; Baker, J. R. HPLC Separation of Different Generations of Poly(amidoamine) Dendrimers Modified with Various Terminal Groups. *Anal. Chem.* **2005**, *77*, 2063–2070.
66. Majoros, I. J.; Keszler, B.; Woehler, S.; Bull, T.; Baker, J. R., Jr. Acetylation of Poly(amidoamine) Dendrimers. *Macromolecules* **2003**, *36*, 5526–5529.
67. Shi, X.; Lesniak, W.; Islam, M. T.; Muniz, M. C.; Balogh, L. P.; Baker, J. R., Jr. Comprehensive Characterization of Surface-Functionalized Poly(amidoamine) Dendrimers with Acetamide, Hydroxyl, and Carboxyl Groups. *Colloids Surf., A* **2006**, *272*, 139–150.
68. Woller, E. K.; Walter, E. D.; Morgan, J. R.; Singel, D. J.; Cloninger, M. J. Altering the Strength of Lectin Binding Interactions and Controlling the Amount of Lectin Clustering Using Mannose/Hydroxyl-Functionalized Dendrimers. *J. Am. Chem. Soc.* **2003**, *125*, 8820–8826.
69. Wiener, E. C.; Konda, S.; Shadron, A.; Brechbiel, M.; Gansow, O. Targeting Dendrimer-Chelates to Tumors and Tumor Cells Expressing the High-Affinity Folate Receptor. *Invest. Radiol.* **1997**, *32*, 748–754.
70. Greeley, J. N.; Meeuwenberg, L. M.; Banaszak Holl, M. M. Surface Infrared Studies of Silicon/Silicon Oxide Interfaces Derived from Hydridosilsesquioxane Clusters. *J. Am. Chem. Soc.* **1998**, *120*, 7776–7782.
71. Lee, S.; Makan, S.; Banaszak Holl, M. M.; McFeely, F. R. Synthetic Control of Solid/Solid Interfaces: Analysis of Three New Silicon/Silicon Oxide Interfaces by Soft X-ray Photoemission. *J. Am. Chem. Soc.* **1994**, *116*, 11819–11826.
72. Twining, B. S.; Baines, S. B.; Fisher, N. S.; Maser, J.; Vogt, S.; Jacobsen, C.; Tovar-Sanchez, A.; Sañudo-Wilhelmy, S. A. Quantifying Trace Elements in Individual Aquatic Protist Cells with a Synchrotron X-ray Fluorescence Microprobe. *Anal. Chem.* **2003**, *75*, 3806–3816.
73. Vogt, S. MAPS: A Set of Software Tools for Analysis and Visualization of 3D X-ray Fluorescence Data Sets. *J. Phys. IV* **2003**, *104*, 635–638.